International Journal of Nanomedicine

Dovepress
open access to scientific and medical research

Open Access Full Text Article

ORIGINAL RESEARCH

Bufalin-Loaded Multifunctional Photothermal Nanoparticles Inhibit the Anaerobic Glycolysis by Targeting SRC-3/HIF-1α Pathway for Improved Mild Photothermal Therapy in CRC

Jing Shang[1,*], Qi Xia[1,*], Yuji Sun[2], Hongtao Wang[2], Jia Chen[1], Yue Li[1], Feng Gao[2], Peihao Yin[1,3,4], Zeting Yuan[1–4]

[1]Interventional Cancer Institute of Chinese Integrative Medicine, Putuo Hospital, Shanghai University of Traditional Chinese Medicine, Shanghai, 200062, People's Republic of China; [2]Shanghai Frontiers Science Center of Optogenetic Techniques for Cell Metabolism, Shanghai Key Laboratory of New Drug Design, School of Pharmacy, East China University of Science and Technology, Shanghai, 200237, People's Republic of China; [3]Shanghai Putuo Central School of Clinical Medicine, Anhui Medical University, Shanghai, 200062, People's Republic of China; [4]The Fifth School of Clinical Medicine, Anhui Medical University, Hefei, 230032, People's Republic of China

*These authors contributed equally to this work

Correspondence: Zeting Yuan; Peihao Yin, Interventional Cancer Institute of Chinese Integrative Medicine, Putuo Hospital, Shanghai University of Traditional Chinese Medicine, Shanghai, 200062, People's Republic of China, Email yuan340202@163.com; yinpeihao@shutcm.edu.cn

Purpose: Compared with traditional photothermal therapy (PTT, >50°C), mild PTT (≤45°C) is a promising strategy for tumor therapy with fewer adverse effects. Unfortunately, its anti-tumor efficacy is hampered by thermoresistance induced by overexpression of heat shock proteins (HSPs). In our previous study, we found bufalin (BU) is a glycolysis inhibitor that depletes HSPs, which is expected to overcome thermotolerance of tumor cells. In this study, BU-loaded multifunctional nanoparticles (NPs) were developed for enhancing the mild PTT of colorectal cancer (CRC).

Methods: Fe_3O_4 NPs coated with the polydopamine (PDA) shell modified with polyethylene glycol (PEG) and cyclic arginine-glycyl-aspartic peptide (cRGD) for loading BU (Fe_3O_4@PDA-PEG-cRGD/BU NPs) were developed. The thermal variations in Fe_3O_4@PDA-PEG-cRGD/BU NPs solution under different conditions were measured. Glycolysis inhibition was evaluated by measuring the glucose uptake, extracellular lactate, and intracellular adenosine triphosphate (ATP) levels. The cellular cytotoxicity of Fe_3O_4@PDA-PEG-cRGD/BU NPs was analyzed using a cell counting kit-8 assay, Calcein-AM/PI double staining, and flow cytometry in HCT116 cells. The magnetic resonance imaging (MRI) performance and anti-tumor therapeutic efficacy of Fe_3O_4@PDA-PEG-cRGD/BU NPs were evaluated in HCT116-tumor bearing mice.

Results: Fe_3O_4@PDA-PEG-cRGD/BU NPs had an average diameter of 260.4±3.5 nm, the zeta potential of –23.8±1.6 mV, the drug loading rate of 1.1%, which had good thermal stability, photothermal conversion efficiencies and MRI performance. In addition, the released BU not only killed tumor cells but also interfered with glycolysis by targeting the steroid receptor coactivator 3 (SRC-3)/HIF-1α pathway, preventing intracellular ATP synthesis, and combating HSP-dependent tumor thermoresistance, ultimately strengthening the thermal sensitivity toward mild PTT both in vitro and in vivo.

Conclusion: This study provides a highly effective strategy for enhancing the therapeutic effects of mild PTT toward tumors.

Keywords: mild photothermal therapy, glycolysis metabolism, bufalin, HIF-1α, SRC-3

Introduction

Colorectal cancer (CRC), a common malignancy of the digestive system, is the third most common cancer and the second leading cause of cancer-related mortality globally.[1] Currently, surgery, chemotherapy, radiotherapy, targeted therapy, and immunotherapy are the primary therapeutic approaches for CRC.[1,2] Nevertheless, approximately half of the patients treated with surgical resection relapse within the first three years.[3] The clinical utility of chemotherapy,

Received: 21 March 2024
Accepted: 8 July 2024
Published: 1 August 2024

Graphical Abstract

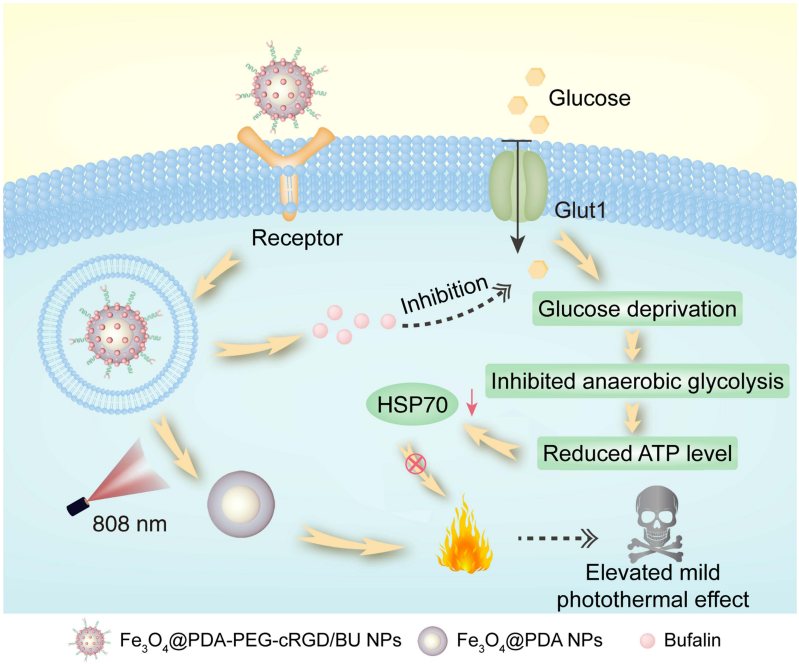

radiotherapy, and targeted therapy is hampered by resistance and cytotoxicity,[4,5] and the various side effects of these remedies, such as gastrointestinal toxicity and other sequelae, inevitably impair the physical quality of life of CRC patients.[6] Immunotherapy is only effective in a few patients, and some can develop acquired resistance.[7] Considering the deficiencies of these conventional therapies, it is imperative to develop effective, specific, and minimally invasive treatment methods for CRC.

Photothermal therapy (PTT) utilizes photothermal agents (PTAs) to convert absorbed light energy into thermal energy to ablate tumor tissues via local hyperthermia (>50°C).[8–10] PTT has attracted considerable interest owing to its low invasive burden, precise spatiotemporal control, and low systemic toxicity.[11,12] Unfortunately, indiscriminate hyperthermia and strong irradiation may inevitably cause serious damage to healthy tissue,[13–15] notably around the vital organs.[10] To circumvent these disadvantages, mild PTT (≤45°C) has been developed.[11,16,17] However, mild temperature PTT activates heat shock responses that prevent thermal damage in cancer cells by overexpressing heat shock proteins (HSPs) such as HSP70 and HSP90, which endow the tumor with heat resistance and severely impair the therapeutic efficacy of mild PTT.[10,18,19] HSPs have been recognized as key factors in heat endurance that initiate cellular anti-apoptotic and cytoprotection pathways.[20] Additionally, HSPs have been related with the CRC progression and reported to use as biomarkers in CRC diagnosis and progression.[21] Consequently, inhibition of HSPs expression in tumor cells has emerged as a critical method for improving the therapeutic efficacy of mild PTT.[22]

HSPs are a conserved family of adenosine triphosphate (ATP)-mediated chaperone proteins whose synthesis, expression, and function primarily rely on intracellular ATP levels.[23,24] As a crucial source of energy in tumor cells, ATP is mainly produced by the glycolysis pathway rather than mitochondrial oxidative phosphorylation even when oxygen is abundant, which is called the Warburg effect.[25,26] Thus, interfering with glycolysis is proposed to reduce glycolytic ATP generation, thereby hampering the expression of HSPs, which significantly elevates mild PTT efficacy against tumors.

Bufalin (BU), a significant monomer component of the traditional Chinese medicine HuaChanSu,[27] exhibits anti-tumor activity against a wide range of cancer types including CRC.[28–32] In our previous study, we established

multifunctional nanoparticles (NPs), cyclo (Arg-Gly-Asp-d-Phe-Cys) [c(RGD)] conjugated Fe_3O_4@polydopamine (PDA) NPs (Fe_3O_4@PDA-PEG-cRGD NPs), with good thermal stability, photothermal conversion efficiencies, and effective anti-tumor effects, which could be further used as an effective platform for integrated PTT and diagnosis of cancer.[33] In such NPs, PDA layer provides a number of advantages, such as a surface for further functionalization with molecules, the excellent biocompatibility and degradability, strong near-infrared (NIR) absorption and high photothermal conversion efficiency, which not only prevent Fe_3O_4 NPs from being cleared from the circulatory system by the immune system but also enhance the photothermal effects of Fe_3O_4 NPs.[34–39] Recently, our previous study found that BU in combination with mild PTT induced by Fe_3O_4@PDA-PEG-cRGD NPs exhibited synergistic anti-tumor effects in CRC cells, but the underlying mechanism was unclear. Our previous investigation confirmed that BU can target steroid receptor coactivator 3 (SRC-3) protein directly.[40–42] In addition, Zhao et al indicated that SRC-3 directly activates HIF transcription and regulates the expression of HIF-1α.[43] More importantly, HIF-1α activates a transcriptional program that upregulates several glycolytic proteins such as glucose transporter 1 (GLUT1), lactate dehydrogenase A (LDHA), and hexokinase 2 (HK2), which facilitates the metabolic shift to aerobic glycolysis.[44,45] Therefore, we hypothesized that BU might improve the anti-tumor effect of mild PTT by suppressing glycolysis via targeting the SRC-3/HIF-1α pathway in CRC.

Thus, we prepared BU-loaded Fe_3O_4@PDA-PEG-cRGD NPs (Fe_3O_4@PDA-PEG-cRGD/BU NPs), which not only improved mild PTT but also achieved magnetic resonance imaging (MRI) both in vitro and in vivo. This nanoplatform could effectively accumulate at tumor sites because of targeting effects, and NIR radiation could trigger the photothermal effect of the Fe_3O_4@PDA-PEG-cRGD NPs and the rapid release of the loaded BU. Subsequently, liberated BU could downregulate the expression of GLUT1 to inhibit glycolysis, and thereby the synthesis of ATP-dependent HSPs was inhibited, which overcame heat resistance. In this study, we provide a promising strategy for specifically sensitizing tumors to mild PTT by rendering a novel Fe_3O_4@PDA-PEG-cRGD/BU NPs nanoplatform.

Materials and Methods

Material

Bufalin (BU, CAS: 465-21-4) was purchased from Chengdu Refines Biotechnology Co., Ltd. Coumarin 6 (C6, HY-N7131) was obtained from MedChemExpress LCC. RPMI 1640 medium, fetal bovine serum (FBS) and penicillin-streptomycin were obtained from Gibco BRL (Carlsbad, CA, USA). The ATP Assay Kit, sodium dodecyl sulfate-polyacrylamide gel electrophoresis (SDS-PAGE) associated reagents, immunostaining fixative, and immunostaining permeate were sourced from Beyotime Biotechnology Co., Ltd (Shanghai, China). The Glucose Uptake Assay Kit, Lactate Assay Kit-WST, Cell Counting Kit-8 (CCK-8), Calcein-AM/PI Double Staining Kit and Annexin V-FITC/PI Apoptosis Detection Kit were purchased from Dojindo (Kumamoto, Japan). Dopamine hydrochloride (DA·HCl) was purchased from Adamas Reagent, Ltd (Shanghai, China), trimethylaminomethane (>99.0%, AR) and hydrochloric acid (36–38%, AR) were purchased from Nanjing Chemical Reagent Co., Ltd (Nanjing, China), and nanometer iron tetroxide dispersion (25% in H_2O, 10–30 nm) was obtained from Macklin Inc. (Shanghai, China). NH_2-PEG-Mal (molecular weight 5000, purity 95%) was obtained from Shanghai Maokang Biological Technology Co., Ltd (Shanghai, China), and anhydrous sodium acetate (>99.0%, AR) and acetic acid (99.5%, AR) were acquired from Shanghai Lingfeng Chemical Reagent Co., Ltd (Shanghai, China). cRGD was obtained from Nanjing Peptide Biotechnology Co., Ltd (Nanjing, China) and NH_2-PEG was procured from Shanghai Yare Biotech, Inc. (Shanghai, China). Primary antibodies against SRC-3, GLUT1, HSP70, and Ki67 were purchased from Abcam (Cambridge, MA, USA). Primary antibodies against HIF-1α and β-actin were obtained from Cell Signaling Technology (Danvers, MA). Primary antibody against LDHA was purchased from Proteintech. The secondary antibodies were obtained from Santa Cruz Biotechnology (Dallas, TX, USA). The SABC-AP immunohistochemical (IHC) staining kit was purchased from Boster Biological Technology Co., Ltd (Wuhan, China) and the terminal deoxynucleotidyl transferase-mediated dUTP Nick-End Labeling (TUNEL) kit was acquired from Roche.

Cell Line and Culture

The human CRC cell line HCT116 was obtained from the Cell Bank of the Chinese Academy of Sciences. HCT116 cells were cultured in RPMI 1640 medium (Gibco) supplemented with 10% FBS (Gibco) and 1% penicillin–streptomycin (Gibco) at 37°C with 5% CO_2.

Animals and Tumor Model

Male BALB/c nude mice (4–6 week, 18–20 g) were purchased from Shanghai Bikaikeyi Biotechnology Co., Ltd., and raised in an SPF room. All experimental protocols followed the ethical animal research guidelines, with the approval of the Animal Ethics Committee of the Putuo District Center Hospital, Shanghai. (Approval No. DWWEC-A-202206005). All animal experiments were performed in accordance with the "Guide for the Care and Use of Laboratory Animals". The tumor was grown by subcutaneous injection of HCT116-luc cells (1×10^7 cells suspended in 0.2 mL PBS) at the right flank of each BALB/c nude mouse under anesthesia. HCT116 tumor-bearing BALB/c nude mice were used for further experiments.

Transcriptome Sequencing and Analysis

Transcriptome sequencing and analyses were performed by OE Biotech (Shanghai, China). Total RNA was extracted using the mirVana miRNA Isolation Kit (Ambion) according to the manufacturer's instructions, and libraries were constructed using the TruSeq Stranded mRNA LTSample Prep Kit (Illumina, San Diego, CA, USA). The libraries were sequenced on an Illumina sequencing platform (Illumina HiSeq X Ten). Differentially expressed genes (DEGs) were identified using the DESeq R package. A p-value <0.05, fold change >2, or fold change <0.5, was set as the threshold for significantly differential expression. Differential expression analysis was performed using the DESeq R package. A p-value <0.05, fold change >2, or fold change <0.5 was set as the threshold for significantly differential expression. GO and KEGG pathway enrichment analyses of DEGs were performed using R based on the hypergeometric distribution.

Western Blot Assay

Proteins were extracted from HCT116 cells treated with different treatments using RIPA lysis buffer containing 1% PMSF. The protein concentration was determined using an enhanced BCA protein assay kit (Beyotime), and all samples were normalized to 2 μg/μL. Equal amounts of cellular proteins were subjected to SDS-PAGE and transferred onto PVDF membranes. The membranes were blocked with 5% skim milk for 1 h at indoor temperature and incubated with antibodies against SRC-3 (1:500), HIF-1α (1:1000), GLUT1 (1:500), LDHA (1:2000), HSP70 (1:1000), and β-actin (1:2000) overnight at 4°C, followed by incubation with the corresponding secondary antibodies for 1 h. The membranes were visualized using a ChemiDoc™ Touch Imaging System (Bio-Rad) and an enhanced chemiluminescence (ECL) kit.

Glycolysis Inhibition Evaluation

Glycolysis inhibition was evaluated by measuring the glucose uptake, extracellular lactate, and intracellular ATP levels. For glucose uptake and extracellular lactate evaluation, HCT116 cells (1.5×10^5 cells/well) were seeded in 96-well plates for 24 h and processed with different treatments. Glucose uptake was quantified using the Glucose Uptake Assay Kit provided by the manufacturer. The supernatant was collected for extracellular lactate determination using the Lactate Assay Kit-WST. For intracellular ATP detection, HCT116 cells were seeded in 24-well plates at a density of 2×10^5 cells/well for 24 h and treated under different conditions. The cells were washed with PBS three times and lysed. The lysate was collected and centrifuged for 5 min (12,000 g) at 4°C. The supernatant was used to measure the intracellular ATP levels using an ATP assay kit. All experiments were performed according to the protocol provided by the manufacturer's instructions.

Characterization and Preparation of Fe_3O_4@PDA-PEG-cRGD/BU NPs

NH_2-PEG-cRGD, Fe_3O_4@PDA, and Fe_3O_4@PDA-PEG-cRGD NPs were synthesized as described in our previous work.[33] The NH_2-PEG-cRGD NPs were verified by ^{1}HNMR. The Fe_3O_4@PDA NPs and Fe_3O_4@PDA-PEG-cRGD

NPs were verified using Fourier transform infrared spectroscopy (FTIR). BU (5 mg) was dissolved in methanol (10 mL) to obtain a 5 mg/mL BU methanol solution. 1 mg of Fe_3O_4@PDA-PEG-cRGD NPs were dissolved in 3.8 mL of deionized water, and 200 μL of 5 mg/mL BU methanol solution was added to the Fe_3O_4@PDA-PEG-cRGD NPs aqueous solution. The mixed solution was ultrasonicated overnight. Fe_3O_4@PDA-PEG-cRGD/BU NPs were obtained by centrifugation at 10,000 rpm for 10 min and verified by UV-vis-NIR. The supernatant was collected to calculate the drug loading (DL) rate and the encapsulation efficiency (EE). The formulas are: DL%= (weight of drug in NPs/weight of total NPs)×100%; EE%=(weight of the drug in NPs)/(weight of the total drug)×100%.

The morphology of the NPs was examined using transmission electron microscopy (TEM, JEM-1400, Tokyo, Japan). The zeta potentials and sizes were measured using a Zetasizer Nano ZS90 (Malvern Instruments, Malvern, UK).

Drug Release from Fe_3O_4@PDA-PEG-cRGD/BU NPs

Fe_3O_4@PDA-PEG-cRGD/BU NPs (1 mg/mL) were added to a dialysis bag (Mw=3500 Da) to investigate their release with or without NIR irradiation at fixed time points. Then, we withdrew 0.1 mL of the nanoparticle solution was withdrawn and replenished with the same volume of the blank solution. The BU content in the collected media was quantified by HPLC.

In vitro and in vivo Photothermal Effect

A series of Fe_3O_4@PDA-PEG-cRGD/BU NPs solutions (0.5 mL) at different concentrations (0, 25, 50, and 100 μg/mL) was exposed to an 808 nm NIR laser (1 W/cm^2) for 5 min. The temperature of the solution was measured every 1 min by an Infrared (IR) thermal-imaging camera. To further determine the thermal stability of Fe_3O_4@PDA-PEG-cRGD/BU NPs, the samples (100 μg/mL, 0.5 mL) were irradiated for 5 min each time, followed by natural cooling to room temperature, and the temperature was recorded every 1 min. This process was repeated five times.

When the tumor volume reached 50 mm^3 approximately, HCT116 tumor-bearing BALB/c nude mice were intravenously injected with PBS, Fe_3O_4@PDA-PEG-cRGD NPs, or Fe_3O_4@PDA-PEG-cRGD/BU NPs. After 24 h, the tumor sites of the mice were irradiated with an 808 nm laser (1 W/cm^2) for 5 min, and real-time thermal images were captured using an IR thermal imaging camera every 1 min.

In vitro and in vivo MRI

For the in vitro MRI experiment, Fe_3O_4@PDA-PEG-cRGD/BU NPs solutions of various concentrations were placed in 1.5 mL eppendorf tubes and vortexed for 3 min. MRI was performed by a 3.0 T magnetic resonance instrument.

For the in vivo MRI study, HCT116 tumor-bearing BALB/c nude mice with a subcutaneous tumor size of 500 mm^3 were intravenously injected with Fe_3O_4@PDA-PEG-cRGD/BU NPs (200 μL, 2 mg/mL). After the injection, the mice were anesthetized and imaged by a 3.0 T magnetic resonance instrument at different times (0, 12, and 24 h). The T_2-weighted MRI parameters were as follows: repetition time (TR), 2500 ms; echo time (TE), 90 ms; field of view (FOV), 100 mm; slice thickness, 3 mm.

Cellular Uptake Experiment

HCT116 cells (3×10^5 cells) were seeded in a confocal dish and cultured for 48 h. Fe_3O_4@PDA-PEG-cRGD NPs labeled with C6 (Fe_3O_4@PDA-PEG-cRGD/C6 NPs) were added and incubated for 2, 4, and 6 h. The RGD pretreatment group was added to further prove the ability of the target of cRGD. Next, the cells were washed three times with PBS, fixed with 4% paraformaldehyde for 15 min, and stained with DAPI dye for 10 min in the dark. Finally, the samples were visualized using confocal laser scanning microscopy (CLSM, Leica, Heidelberg, Germany).

Cytotoxicity Assay

The cytotoxicity of Fe_3O_4@PDA-PEG-cRGD NPs and Fe_3O_4@PDA-PEG-cRGD/BU NPs was estimated in HCT116 cells using the CCK-8 assay. In brief, HCT116 cells (1.5×10^5 cells/well) were seeded in 96-well plates and cultured for 24 h. HCT116 cells were then incubated with Fe_3O_4@PDA-PEG-cRGD NPs and Fe_3O_4@PDA-PEG-cRGD/BU NPs at

different concentrations and irradiated with or without an 808 nm laser (1.0 W/cm^2) for 5 min. The culture medium was replaced with fresh culture medium and incubated for another 24 h. Finally, the culture medium was discarded and replaced with fresh culture medium containing 10% CCK-8. After for 1–2 h of incubation, optical density was measured using a multifunctional microplate reader (Varioskan LUX; Thermo Fisher Scientific) at OD_{450}.

The cell apoptosis of HCT116 cells treated with different treatments were visualized through Calcein-AM/PI Double Staining Kit and Annexin V-FITC/PI Apoptosis Detection Kit. HCT116 cells were seeded in 24-well plates at a density of 2×10^5 cells/well and allowed to adhere to culture plate overnight. The cells were then treated with PBS, Fe_3O_4@PDA-PEG-cRGD NPs, BU, Fe_3O_4@PDA-PEG-cRGD/BU NPs, Fe_3O_4@PDA-PEG-cRGD NPs+NIR and Fe_3O_4@PDA-PEG-cRGD/BU NPs+NIR. The NIR groups were radiated with 808 nm laser (1.0 W/cm^2) for 5 min. Then, all culture medium was replaced. After another 24 h of incubation, the cells were digested with ethylenediaminetetraacetic acid-free trypsin and washed with cold PBS three times. Finally, the cells were stained with Calcein-AM/PI or Annexin V-FITC/PI, and detected by fluorescence microscopy and flow cytometry, respectively.

In vivo Anti-Tumor Efficacy

When the tumor size reached 50 mm^3, the mice were randomly divided into six groups (six mice per group): (1) control, (2) Fe_3O_4@PDA-PEG-cRGD NPs, (3) BU, (4) Fe_3O_4@PDA-PEG-cRGD/BU NPs, (5) Fe_3O_4@PDA-PEG-cRGD NPs +NIR, and (6) Fe_3O_4@PDA-PEG-cRGD/BU NPs+NIR. All mice were injected via the tail vein on the days 0, 2, and 4. The mice in the NIR groups were irradiated for 5 min with an 808 nm laser (1 W/cm^2) on the days 1, 3, and 5. After treatment, the tumor volume and body weight were recorded every 2 days, and an ex vivo imaging system (IVIS, PerkinElmer) was used before sacrifice. Tumor volume was calculated according to the following formula: $V = a\times b^2\times\frac{\pi}{6}$ (mm^3), where a is the major axis and b is the minor axis of the tumor. When the treatment was completed, the mice were sacrificed, and the tumors and major organs (heart, liver, spleen, lung, and kidney) were harvested. The main organs were examined using hematoxylin and eosin (H&E) staining. Serum levels of aspartate aminotransferase (AST), alanine aminotransferase (ALT), serum creatinine (CRE), and urea nitrogen (BUN) were measured using assay kits purchased from the Jiancheng Bioengineering Institute (Nanjing, China). Moreover, the tumor tissues were treated with IHC staining and TUNEL staining to evaluate the anti-tumor mechanism. For animal welfare, the mice were sacrificed when the tumor volume reached 1500 mm^3.

Statistical Analysis

Statistical analysis was performed using GraphPad Prism software (version 8.0) via one-way analysis of variance (ANOVA) and Student's unpaired *t*-test, and the results are shown as mean ±SD. Statistical significance was set at $P<0.05$.

Results

BU Inhibited Glycolysis by Targeting the SRC-3/HIF-1α Pathway

To investigate the effect of BU on the human CRC HCT116 cell line, cell viability was evaluated using the CCK-8 assay, and a safe BU concentration (IC_{20}, 5 nM) was chosen for further experiments (Figure S1). To clarify the effects of BU on glycolysis, transcriptome sequencing of HCT116 cells was performed after treatment with BU for 48 h, and DEGs were screened (Figure 1A). We performed GO term and KEGG pathway enrichment analyses to further elucidate the functions of the DEGs. GO term enrichment analysis indicated that these DEGs were mainly involved in response to hypoxia and glycolytic processes (Figure 1B). Similarly, KEGG pathway enrichment analysis revealed that HIF-1 and glycolysis signaling pathways were significantly altered (Figure 1C). Subsequently, our Western blot assay results validated that BU downregulated the expression of HIF-1α, the main regulatory subunit of HIF-1 activity, and its target genes of glycolysis in HCT116 cells including GLUT1 and LDHA (Figure 1D). Specific glycolytic parameters were measured to confirm the inhibitory effect of BU. Glucose uptake (Figure 1E), extracellular lactate (Figure 1F), and intracellular ATP levels (Figure 1G) also decreased in HCT116 cells in a dose-dependent manner post BU treatment. As previously reported, BU can directly target the SRC-3 protein[42] and HIF-1α expression is regulated by SRC-3.[43] We also detected the expression

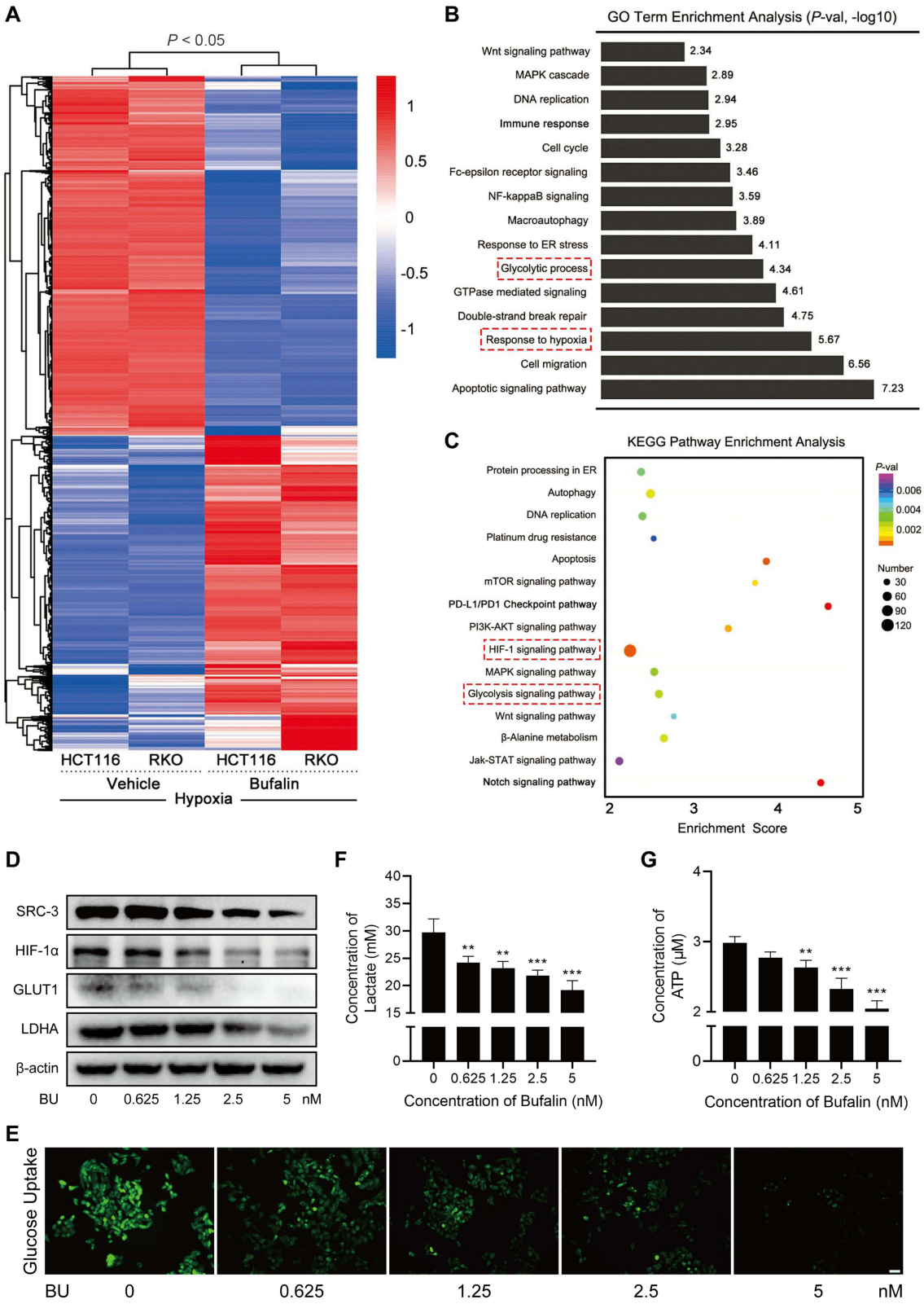

Figure 1 BU inhibited glycolysis by targeting the SRC-3/HIF-1α pathway. (**A**) Expression heat map of DEGs in HCT116 cells and RKO cells post BU treatment under hypoxia. (**B**) GO enrichment analysis of DEGs in HCT116 cells and RKO cells post BU treatment under hypoxia; the top 15 biological processes are listed. (**C**) KEGG pathway enrichment analysis of DEGs in HCT116 cells and RKO cells post BU treatment under hypoxia. (**D**) Western blot analysis of SRC-3, HIF-1α, GLUT1, LDHA and β-actin expression in HCT116 cells incubated with different BU concentrations. (**E**) Glucose uptake level (scale bar=50 μm), (**F**) the extracellular lactate content and (**G**) the intracellular ATP level in HCT116 cells after being treated with different concentrations of BU. (n=3). ***P*<0.01, ****P*<0.001.

https://doi.org/10.2147/IJN.S470005 DovePress

of SRC-3 by Western blot and found that BU could inhibit SRC-3 expression in a dose-dependent manner (Figure 1D). Taken together, these results indicate that BU inhibits glycolysis by targeting the SRC-3/HIF-1α signaling pathway.

BU Enhanced Mild PTT by Downregulating HSP70 Expression

It is well known that HSPs induced by heat shock responses confer thermotolerance in mild PTT and protect tumor cells from apoptosis, eventually leading to the failure of mild PTT. First, HCT116 cells were co-incubated with Fe_3O_4@PDA-PEG-cRGD NPs for 4 h, irradiated with an 808 nm laser (1 W/cm^2), and maintained at various temperatures (37°C, 39°C, 41°C, 43°C, and 45°C) for 5 min. As shown in Figure S2, mild temperatures in the range of 37–45°C could increase the expression of HSP70 in HCT116 cells. The ability of BU to downregulate HSP70 expression in HCT116 cells was further examined by Western blot, and the results showed that BU could downregulate the expression of HSP70 (Figure S3), which suggests that BU might potentiate the therapeutic efficacy of mild PTT against CRC by inhibiting HSP70 expression.

Based on the capacity of BU to downregulate HSP70 expression, we performed a combination therapy with BU and mild PTT. First, the CCK-8 assay was conducted, and the results showed that BU sensitized the cells to the cytotoxicity of mild PTT, indicating a synergistic effect between BU and mild PTT (Figure 2A). Second, to investigate the underlying mechanism that BU improves the efficacy of mild PTT, several tests were performed. As shown in Figure 2B, Western blot assay showed that the protein expression levels of HSP70 increased in the mild PTT group and significantly decreased after treatment with BU. In addition, glycolysis-related proteins such as GLUT1 and LDHA were down-regulated in the combination group (Figure 2B). Correspondingly, the levels of glucose uptake (Figure 2C), extracellular lactate (Figure 2D), and intracellular ATP (Figure 2E) significantly decreased in the free BU and BU combination groups. These findings collectively indicate that blocking the expression of HSPs by inhibiting ATP generation via BU-mediated glycolysis suppression could effectively amplify the sensitivity of CRC towards mild PTT.

Preparation and Characterization of Fe_3O_4@PDA-PEG-cRGD/BU NPs

The ability of BU to downregulate HSP70 expression and improve the effects of mild PTT has been confirmed. However, its low water solubility, short half-life, and serious toxicity limit its application.[46–48] To effectively deliver BU to the tumors to obtain ideal drug accumulation and avoid possible side effects, Fe_3O_4@PDA-PEG-cRGD/BU NPs were prepared by adsorbing BU onto the surface of the NPs through π–π conjugation between BU and PDA, and its synthetic route illustrated in Figure 3A.

Fe_3O_4@PDA NPs, NH_2-PEG-cRGD NPs, and Fe_3O_4@PDA-PEG-cRGD NPs were synthesized as previously described methods.[33] As shown in Figure 3B, the successful synthesis of NH_2-PEG-cRGD NPs were identified by ^{1}HNMR spectrum. The FTIR results indicated that Fe_3O_4@PDA NPs and Fe_3O_4@PDA-PEG-cRGD NPs were successfully synthesized (Figure 3C). Fe_3O_4@PDA-PEG-cRGD/BU NPs displayed a typical core–shell structure and had average diameters of approximately 260.4±3.5 nm (Figure 3D). As indicated in Table 1, the zeta potential of Fe_3O_4@PDA-PEG-cRGD/BU NPs was −23.8±1.6 mV and the drug loading efficacies (DL%) were 1.1%. In addition, the UV-vis-NIR results showed that the characteristic peak of BU appeared in the absorption curve of Fe_3O_4@PDA-PEG-cRGD/BU NPs, confirming the presence of BU in the nanosystem (Figure 3E). Next, the cumulative release of BU with or without NIR irradiation was determined. As shown in Figure 3F, the cumulative release rate of BU in Fe_3O_4@PDA-PEG-cRGD/BU NPs monitored in the tumor simulation microenvironment (pH 5.0) was attained 90.61±1.38% within 72 h with NIR laser irradiation. As stated above, Fe_3O_4@PDA-PEG-cRGD/BU NPs are successfully structured and exhibit the desired NIR-responsive drug release behavior.

Subsequently, the photothermal properties of Fe_3O_4@PDA-PEG-cRGD/BU NPs were evaluated. As shown in Figure 3G and H, the Fe_3O_4@PDA-PEG-cRGD/BU NPs aqueous solution exhibited a time- and concentration-dependent photothermal effect under continuous 808 nm NIR irradiation (1 W/cm^2, 5 min). Furthermore, heating and cooling cycle experiments using NIR irradiation were performed to evaluate the photothermal stability of Fe_3O_4@PDA-PEG-cRGD/BU NPs, and the heat-generation ability remained stable at the end of the fifth cycle (Figure 3I). These results confirm the outstanding photothermal performance of the Fe_3O_4@PDA-PEG-cRGD/BU NPs.

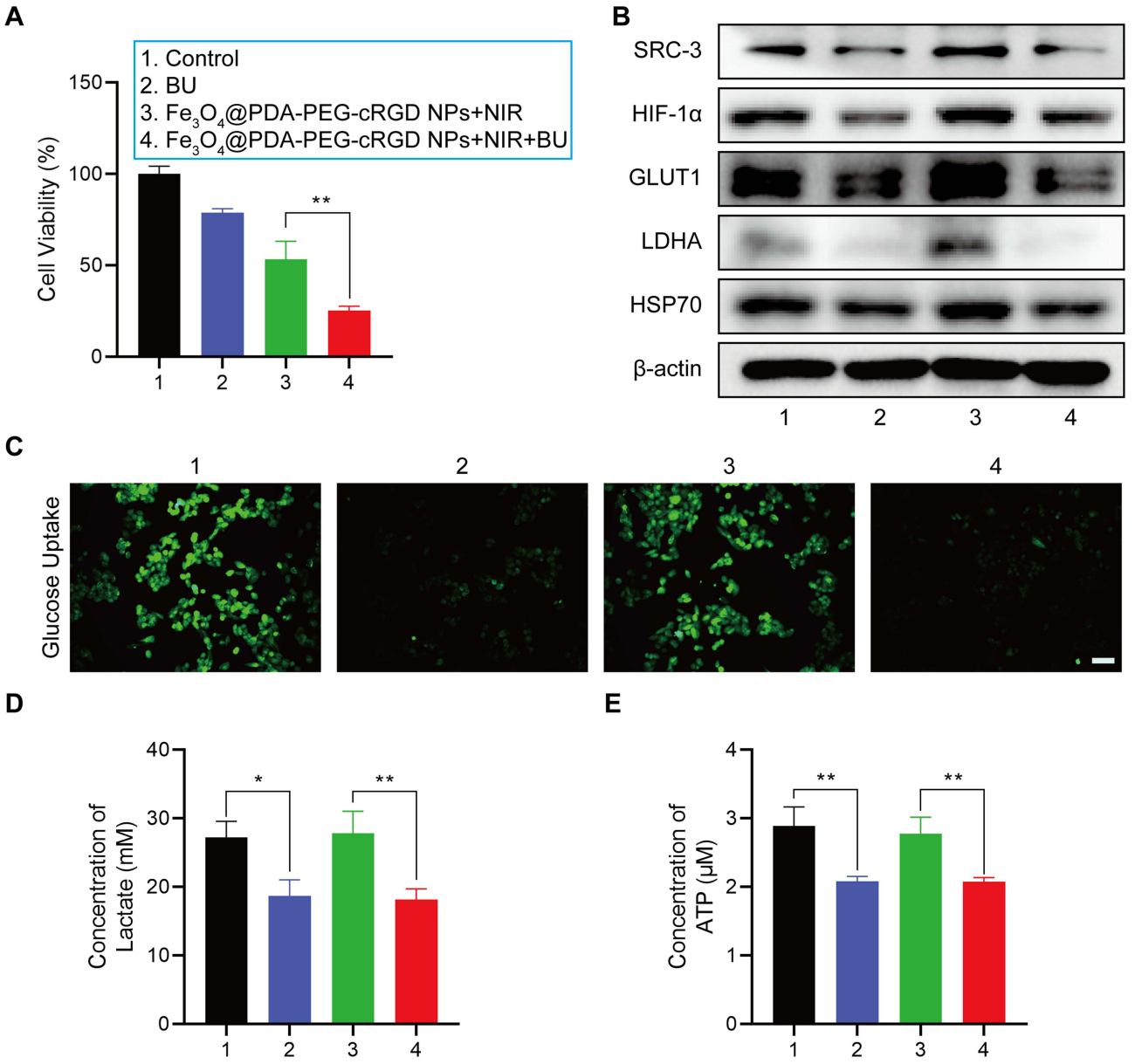

Figure 2 BU enhanced mild PTT by down-regulating HSP70 expression. (**A**) Cytotoxicity of BU in combination with mild PTT on HCT116 by CCK-8. (**B**) SRC-3, HIF-1α, GLUT1, LDHA, HSP70 and β-actin protein expression on HCT116 cells treated with BU in combination with mild PTT by Western blot. (**C**) Glucose uptake level (scale bar=50 μm), (**D**) the extracellular lactate content and (**E**) the intracellular ATP level in HCT116 cells after being treated with BU in combination with mild PTT. (n=3). **P*<0.05, ***P*<0.01.

Cellular Uptake and Glycolysis Inhibition

For cellular uptake, Fe_3O_4@PDA-PEG-cRGD/C6 NPs were used to evaluate the uptake levels in HCT116 cells by CLSM. As shown in Figure 4A, the green fluorescence signals became more stable over time, indicating that Fe_3O_4@PDA-PEG-cRGD NPs were efficiently taken up by the HCT116 cells. After pre-incubation with the free RGD peptide, the cellular uptake levels of Fe_3O_4@PDA-PEG-cRGD/C6 NPs were reduced, which might be due to the competitive binding of integrin $\alpha_v\beta_3$ to free RGD and demonstrated that cRGD could specifically target the highly expressed integrin $\alpha_v\beta_3$ in HCT116 cells (Figure S4).

After specific internalization by HCT116 cells, the effect of the Fe_3O_4@PDA-PEG-cRGD/BU NPs on glycolysis was investigated. As shown in Figure 4B, Western blot analysis confirmed that Fe_3O_4@PDA-PEG-cRGD/BU NPs with or without NIR suppressed SRC-3, HIF-1α, GLUT1, and LDHA expression, consistent with free BU. The results for

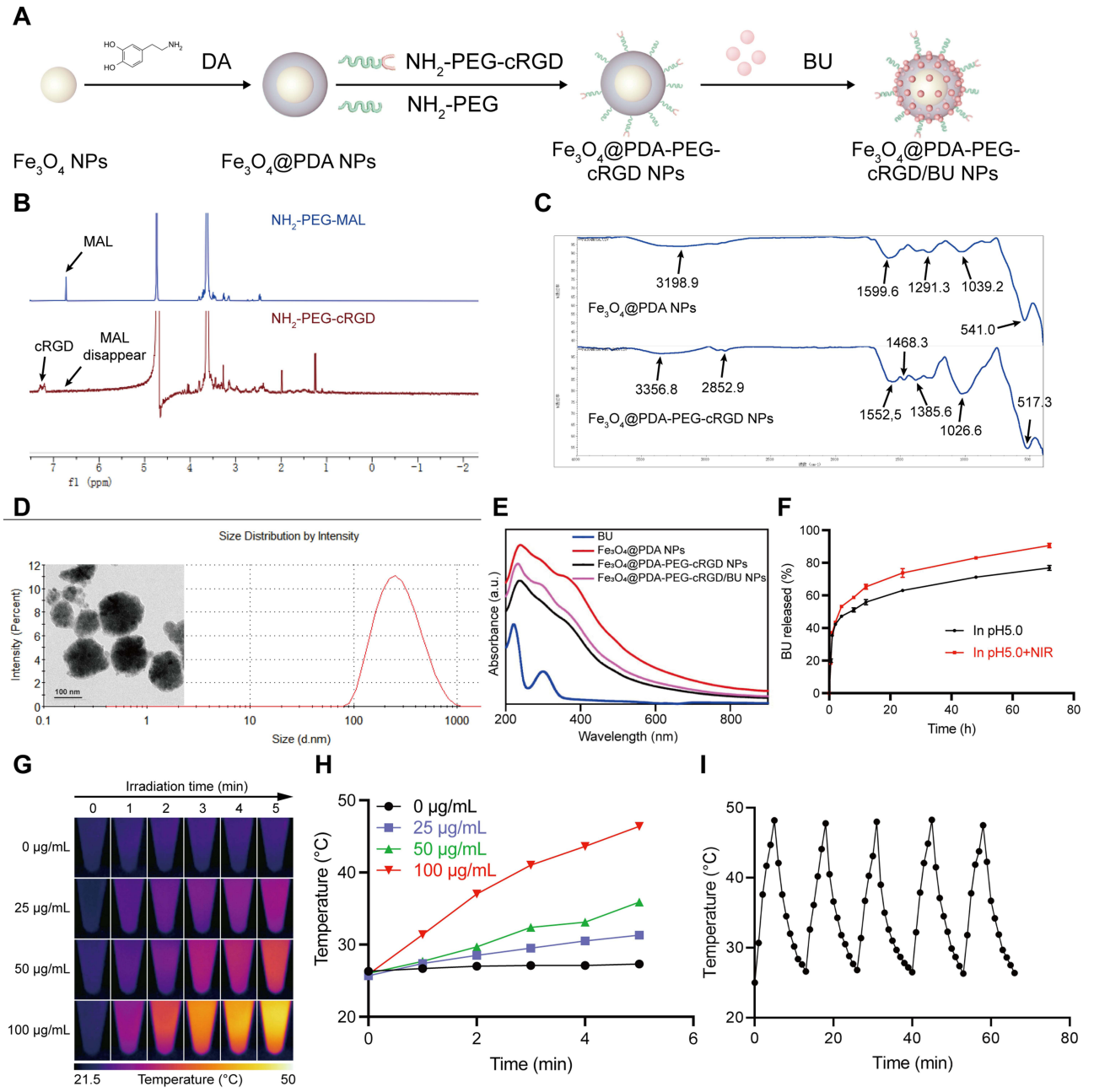

Figure 3 Preparation and Characterization of Fe_3O_4@PDA-PEG-cRGD/BU NPs. (**A**) Schematic illustration of preparation of Fe_3O_4@PDA-PEG-cRGD/BU NPs. (**B**) ^{1}HNMR results of NH_2-PEG-MAL NPs and NH_2-PEG-cRGD NPs. (**C**) FTIR results of Fe_3O_4@PDA NPs and Fe_3O_4@PDA-PEG-cRGD NPs. (**D**) Size distribution and TEM image of Fe_3O_4@PDA-PEG-cRGD/BU NPs. (**E**) UV-vis-NIR absorption spectrum of different NPs. (**F**) BU release profile of Fe_3O_4@PDA-PEG-cRGD/BU NPs under different conditions. (**G**) Thermal images and (**H**) temperature curves of different concentrations of Fe_3O_4@PDA-PEG-cRGD/BU NPs under 808 nm laser irradiation at 1 W/cm^2. (**I**) Temperature evolution of Fe_3O_4@PDA-PEG-cRGD/BU NPs aqueous solution under NIR irradiation (1.0 W/cm^2) after five laser on/off cycles.

glucose uptake (Figure 4C), extracellular lactate (Figure 4D), and intracellular ATP (Figure 4E) further confirmed that Fe_3O_4@PDA-PEG-cRGD/BU NPs suppressed glycolysis in HCT116 cells. Moreover, Fe_3O_4@PDA-PEG-cRGD NPs with NIR effectively upregulated HSP70 expression, whereas Fe_3O_4@PDA-PEG-cRGD/BU NPs with NIR significantly downregulated the expression level of HSP70 in HCT116 cells (Figure 4B). Our findings show that Fe_3O_4@PDA-PEG-cRGD/BU NPs inhibit glycolysis and ultimately block ATP-dependent HSPs synthesis.

Table 1 Physicochemical Property of Fe_3O_4@PDA-PEG-cRGD/BU NPs

	Fe_3O_4@PDA-PEG-cRGD/BU NPs
DL%	1.1%
EE%	12.05%
Size (nm)	260.4±3.5
Zeta potential (mV)	–23.8±1.6
PDI	0.26

In vitro Anticancer Cytotoxicity

Next, we evaluated the therapeutic efficacy of the Fe_3O_4@PDA-PEG-cRGD/BU NPs in HCT116 cells. The CCK-8 assay was used to measure the toxicity of different NPs. As illustrated in Figure 5A, there was no obvious cytotoxicity, even at the highest therapeutic concentration, regardless of the type of NPs without NIR, indicating the excellent biocompatibility of our designed nanoplatform. The relative viability of the group with NIR was significantly lower than that of the corresponding group without NIR, especially the Fe_3O_4@PDA-PEG-cRGD/BU NPs with NIR (Figure 5B). A live/dead assay was performed using the calcein-AM/PI double staining kit to further visualize the therapeutic efficacy of the Fe_3O_4@PDA-PEG-cRGD/BU NPs. As shown in Figure 5C, HCT116 cells treated with Fe_3O_4@PDA-PEG-cRGD NPs plus NIR showed slightly more dead cells (red fluorescence) than the control group, suggesting a limited therapeutic effect induced by mild PTT. Strikingly, HCT116 cells in the Fe_3O_4@PDA-PEG-cRGD/BU NPs with NIR displayed the best therapeutic efficacy compared to the other groups, authorized by the largest number of dead cells. In contrast, cell death in the BU, Fe_3O_4@PDA-PEG-cRGD NPs, and Fe_3O_4@PDA-PEG-cRGD/BU NPs groups was negligible. This finding was also supported by flow cytometry using the Annexin V-FITC/PI Apoptosis Detection Kit. As shown in Figure 5D and E, the apoptosis rate of HCT116 cells treated with Fe_3O_4@PDA-PEG-cRGD/BU NPs plus NIR was higher than that of other groups. Our findings showed that Fe_3O_4@PDA-PEG-cRGD/BU NPs overcome photothermal resistance and significantly improve the efficiency of mild PTT.

Magnetic Properties and MRI

A vibration sample magnetometer (VSM) was used at room temperature to verify the magnetic properties. As shown in Figure 6A, Fe_3O_4 NPs and Fe_3O_4@PDA-PEG-cRGD/BU NPs were superparamagnetic because there was no evident remanence or coercivity at 300 K. The saturation magnetization values for the Fe_3O_4 NPs and Fe_3O_4@PDA-PEG-cRGD /BU NPs were approximately 44.90 emu/g and 42.95 emu/g, respectively. Although the saturation magnetization decreased, the Fe_3O_4@PDA-PEG-cRGD/BU NPs could still be easily enriched within 1 min using a magnet (Figure 6B). These results suggest that Fe_3O_4@PDA-PEG-cRGD/BU NPs retain their superparamagnetic properties and exhibit outstanding magnetic field responsivity, making them suitable for MRI applications.

To further evaluate the potential of Fe_3O_4@PDA-PEG-cRGD/BU NPs for MRI, the MRI signals of Fe_3O_4@PDA-PEG-cRGD/BU NPs were observed both in vitro and in vivo. As shown in Figure 6C, the measured T_2-weighted MRI of the Fe_3O_4@PDA-PEG-cRGD/BU NPs dispersions exhibited an obvious darkening effect with increasing Fe concentration. We then examined the MRI capabilities in vivo. As shown in Figure 6D, the T_2-weighted MRI intensity in the tumor area visibly increased as the circulation time increased, especially 24 h after tail vein injection, verifying that the NPs could aggregate at the tumor site. These results suggest that Fe_3O_4@PDA-PEG-cRGD/BU NPs could serve as promising contrast agents for MRI.

In vivo Synergistic Therapy and Biosafety Assessment

The photothermal conversion efficiency of Fe_3O_4@PDA-PEG-cRGD/BU NPs was explored in HCT116 tumor-bearing BALB/c nude mice. At 24 h post-intravenous injection, the mice were exposed to NIR (1 W/cm^2, 5 min), and the

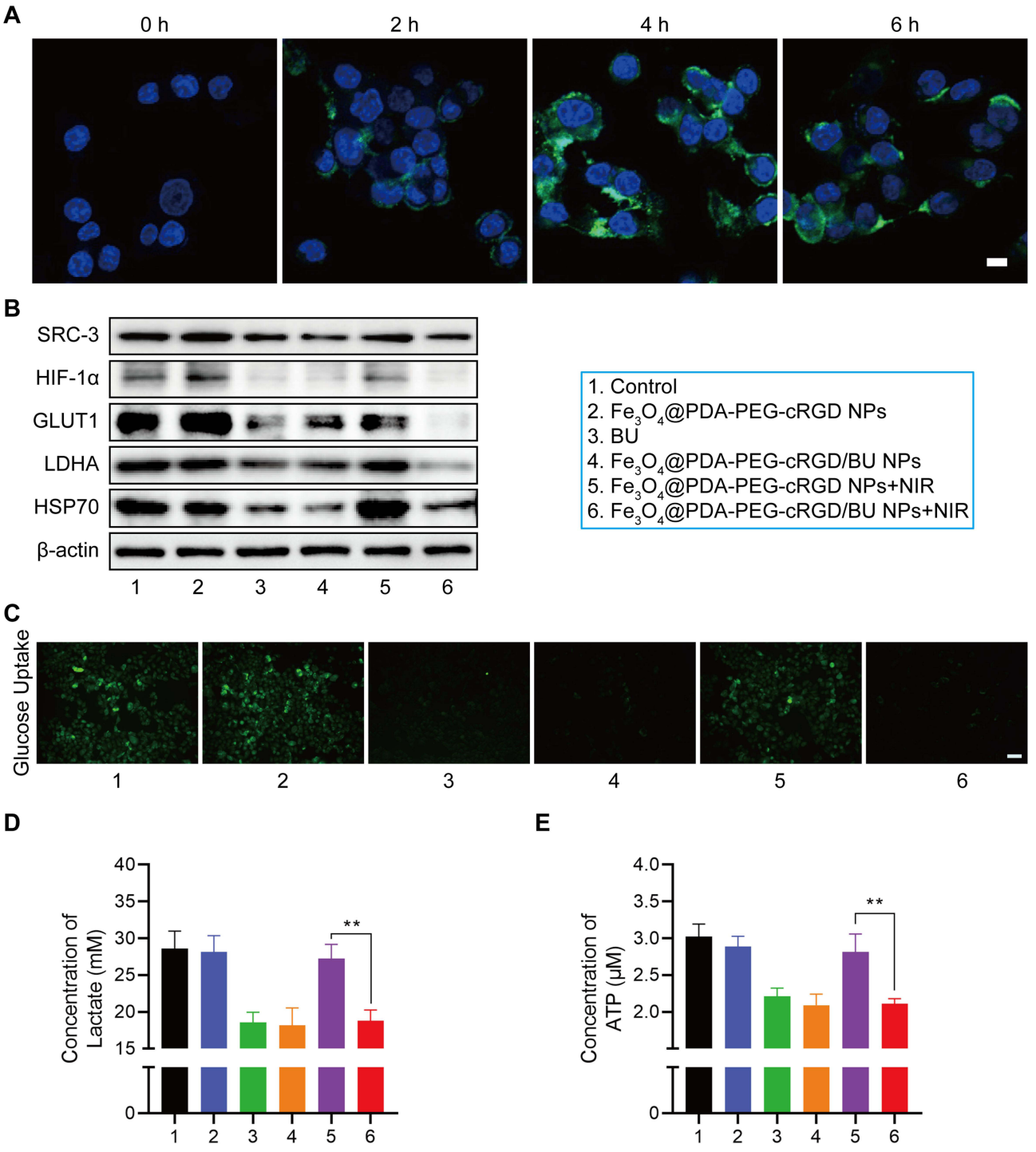

Figure 4 Cellular uptake and glycolysis inhibition. (**A**) The CLSM images of HCT116 cells after being treated with Fe_3O_4@PDA-PEG-cRGD/C6 NPs for 0, 2, 4 and 6 h (scale bar=20 μm). (**B**) SRC-3, HIF-1α, GLUT1, LDHA, HSP70 and β-actin protein expression on HCT116 cells treated with different formulations determined by Western blot. (**C**) Glucose uptake level (scale bar=50 μm), (**D**) the extracellular lactate content and (**E**) the intracellular ATP level in HCT116 cells after different treatments. (n=3). $^{**}P<0.01$.

temperature at the tumor surface was recorded using an IR thermal imaging camera. As shown in Figure 7A and B, the tumor temperature in the Fe_3O_4@PDA-PEG-cRGD NPs and Fe_3O_4@PDA-PEG-cRGD/BU NPs groups reached approximately 45°C, while the temperature in the PBS group only exhibited a tender increase under the same irradiation conditions. Therefore, Fe_3O_4@PDA-PEG-cRGD/BU NPs are ideal PTAs for mild PTT in vivo.

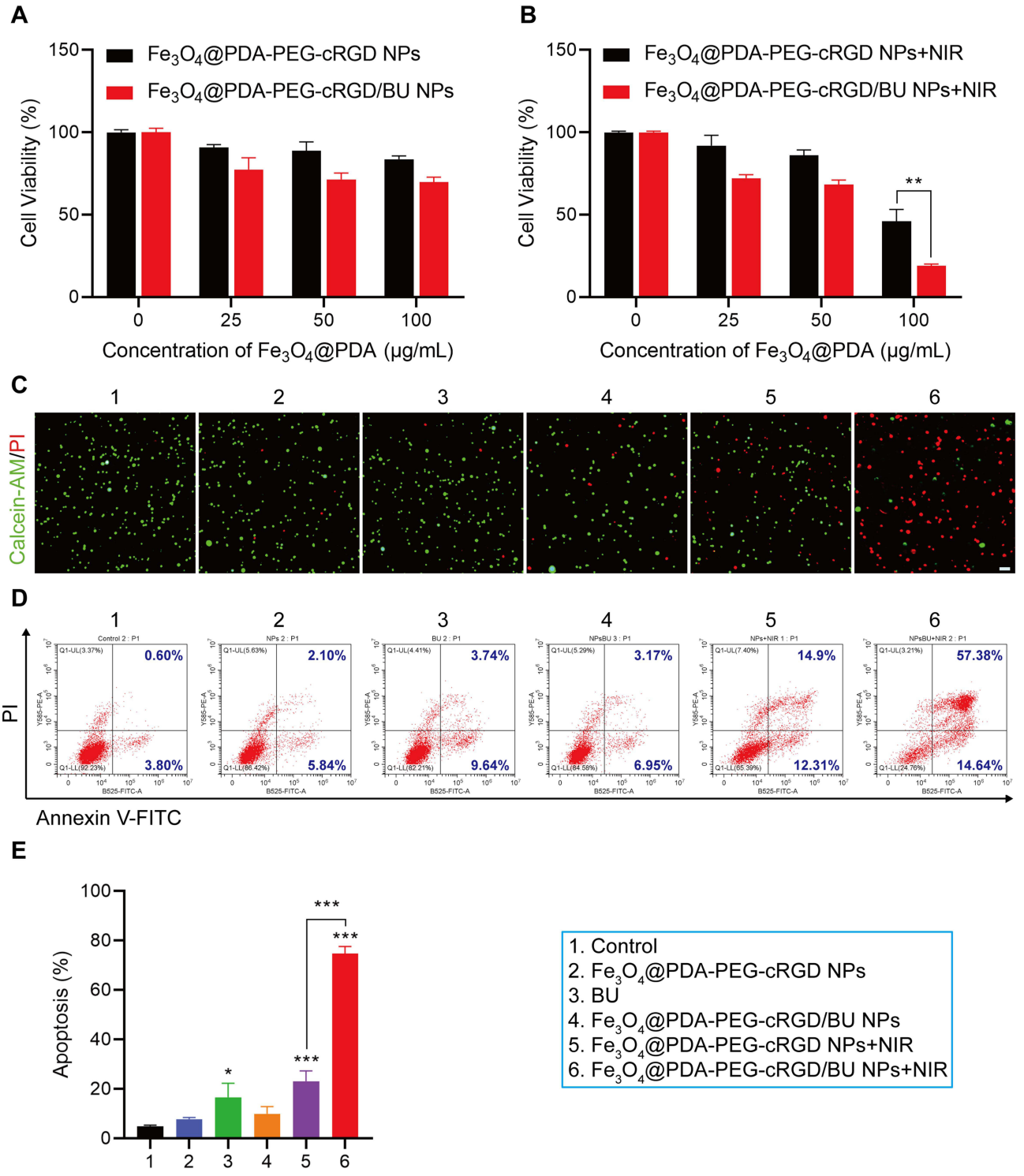

Figure 5 In vitro anticancer cytotoxicity. (**A**) Cytotoxicity of Fe_3O_4@PDA-PEG-cRGD NPs and Fe_3O_4@PDA-PEG-cRGD/BU NPs without NIR irradiation against HCT116 cells. (**B**) Cytotoxicity of Fe_3O_4@PDA-PEG-cRGD NPs and Fe_3O_4@PDA-PEG-cRGD/BU NPs with NIR irradiation against HCT116 cells. (**C**) Inverted fluorescence microscope images of live/dead double staining of HCT116 cells treated with various formulations (scale bar=20 μm). (**D**) Apoptosis rates of HCT116 cells treated with different formulations determined by flow cytometry. (**E**) Relative apoptosis rates after different formulations treatments. (n=3). *P<0.05, **P<0.01, ***P<0.001.

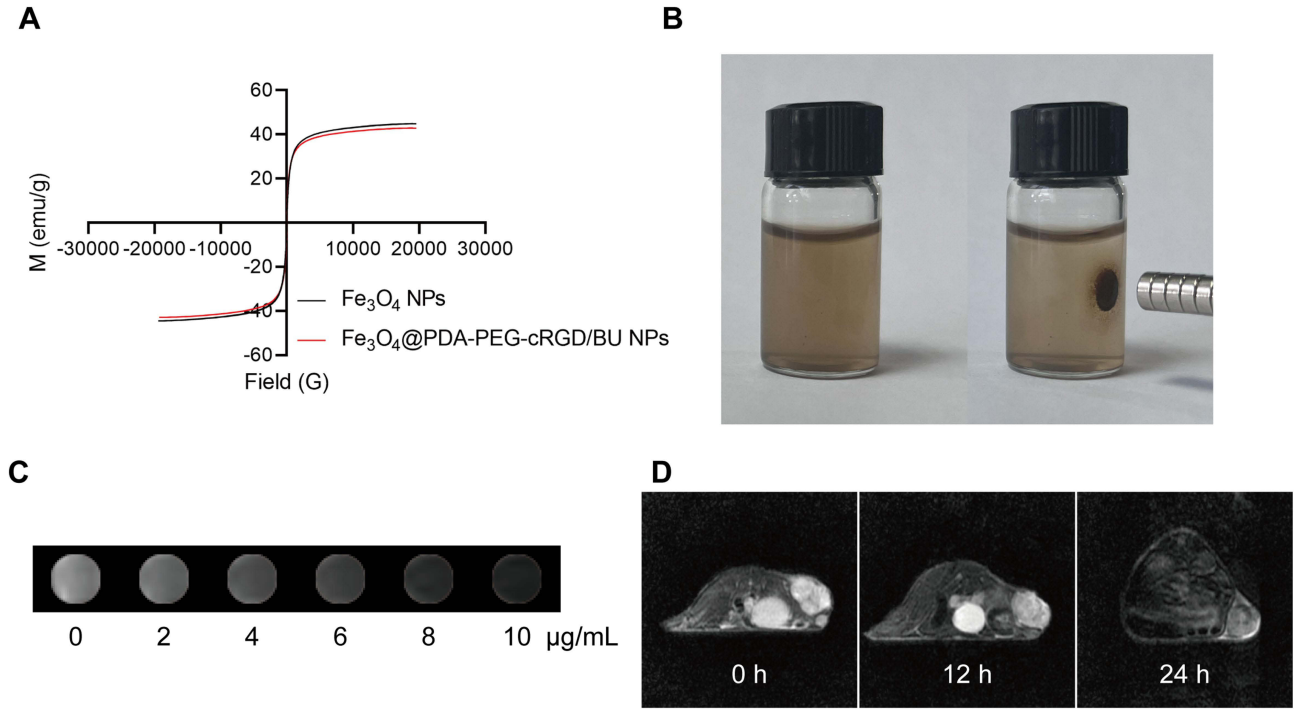

Figure 6 Magnetic Properties and MRI. (**A**) Magnetic hysteresis curves of Fe_3O_4 NPs and Fe_3O_4@PDA-PEG-cRGD/BU NPs at 300K. (**B**) Photographs of Fe_3O_4@PDA-PEG -cRGD/BU NPs solutions in the absence and presence of a magnetic field. (**C**) T_2-weighted MRI of Fe_3O_4@PDA-PEG-cRGD/BU NPs in vitro. (**D**) T_2-weighted MRI of mice after intravenous injection of Fe_3O_4@PDA-PEG-cRGD/BU NPs in vivo at 0, 12 and 24 h.

Finally, we established HCT116 tumor-bearing BALB/c nude mice to evaluate the mild PTT efficacy. After the tumor volume reached approximately 50 mm^3, nude mice were randomly divided into six groups and treated with (1) control, (2) Fe_3O_4@PDA-PEG-cRGD NPs, (3) BU, (4) Fe_3O_4@PDA-PEG-cRGD/BU NPs, (5) Fe_3O_4@PDA-PEG-cRGD NPs +NIR, and (6) Fe_3O_4@PDA-PEG-cRGD/BU NPs+NIR. The experimental process in vivo was illustrated in Figure 7C. As shown in Figure 7D and E, Fe_3O_4@PDA-PEG-cRGD/BU NPs+NIR treatment significantly inhibited tumor growth (84.63%), followed by Fe_3O_4@PDA-PEG-cRGD NPs+NIR treatment (59.32%). In contrast, a negligible anti-tumor effect was observed in other groups. At the endpoint, the mice were euthanized, and the tumor tissues and major organs were harvested for further analysis. IHC staining results showed that the Fe_3O_4@PDA-PEG-cRGD/BU NPs+NIR group had significantly reduced levels of SRC-3 (Figure S5A), HIF-1α (Figure S5B), GLUT1 (Figure 7F), and LDHA (Figure 7G) in the tumors, thereby further confirming the results in vitro that BU could inhibit glycolysis via targeting SRC-3/HIF-1α pathway. Interestingly, HSP70 (Figure 7H) was markedly upregulated in the Fe_3O_4@PDA-PEG-cRGD NPs+NIR group, whereas it dramatically decreased in the Fe_3O_4@PDA-PEG-cRGD/BU NPs+NIR group, suggesting that BU could promote mild PTT efficacy by repressing HSP70 expression. Furthermore, the suppression of tumor proliferation was confirmed by Ki67 staining (Figure 7I) and TUNEL staining (Figure 7J), indicating that Fe_3O_4@PDA-PEG-cRGD/BU NPs+NIR effectively inhibited tumor growth. Taken together, these results confirm the cooperative anticancer potency of glycolysis suppression and mild PTT.

Importantly, the body weight of the treated mice did not change significantly during treatment (Figure 8A), demonstrating the favorable biocompatibility of Fe_3O_4@PDA-PEG-cRGD/BU NPs. In addition, the major organs were stained with H&E, and the results showed no evident physiological or morphological changes (Figure 8B). Furthermore, the liver and kidney function indexes including ALT, AST, BUN, and CRE were within normal ranges (Figure S6). Taken together, these findings indicate that Fe_3O_4@PDA-PEG-cRGD/BU NPs can be safely used for mild PTT without generating evident systemic toxicity.

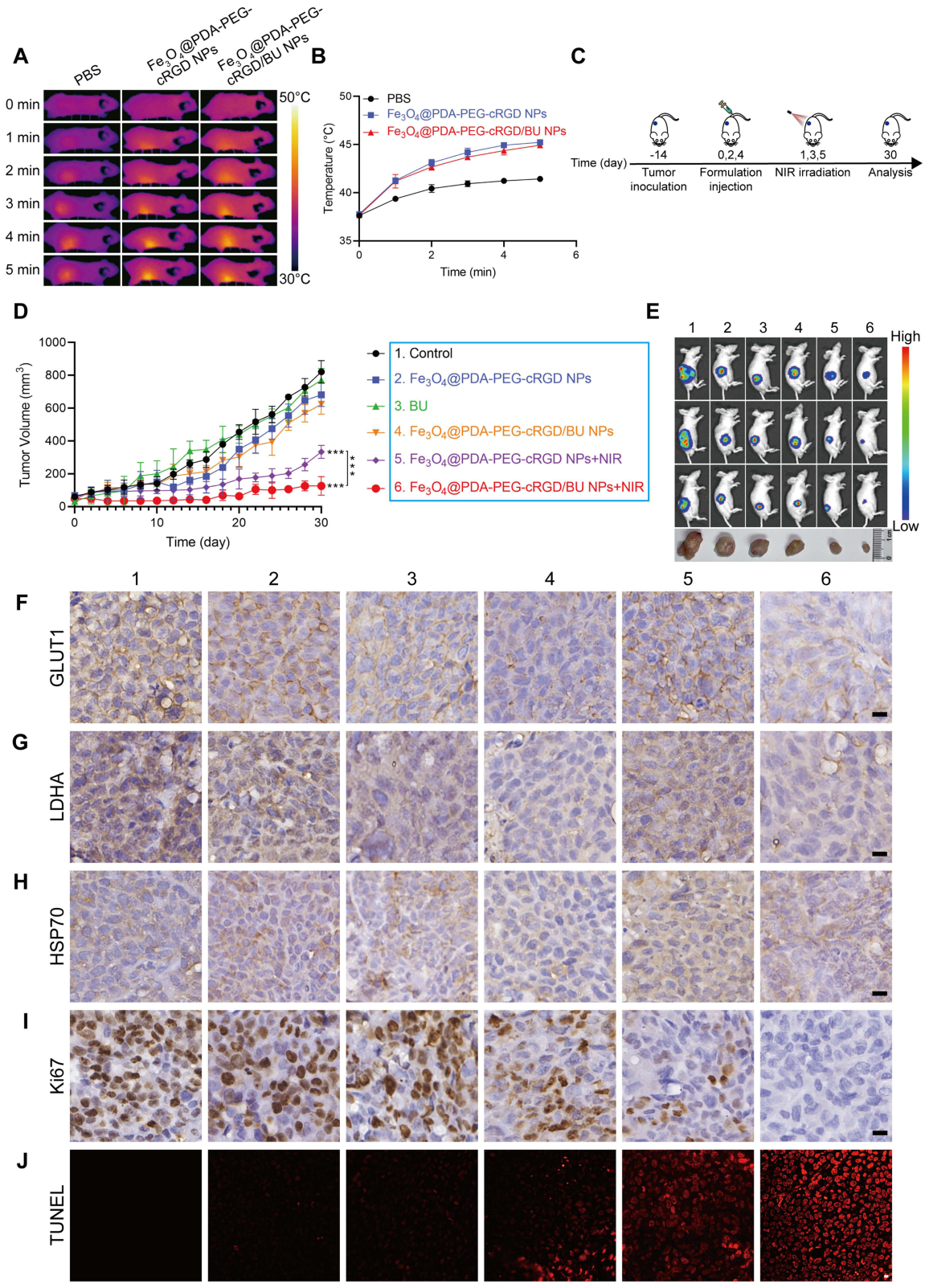

Figure 7 In vivo synergistic therapy. (**A**) The photothermal images and (**B**) the temperature changes curves of different drug treated groups after irradiation with 808 nm NIR laser (1 W/cm^2). (**C**) Schematic illustration of the experiment design to examine the anti-tumor effect in vivo. (**D**) Tumor volume changes in all groups during treatments. (**E**) Bioluminescence images of HCT116-luc cells in mice body before sacrificing and respective photographs of tumor. IHC for (**F**) GLUT1, (**G**) LDHA, (**H**) HSP70 and (**I**) Ki67 and immunofluorescence staining for (**J**) TUNEL assay of tumors after different treatments (scale bar=10 μm). (n=6). ***P<0.001.

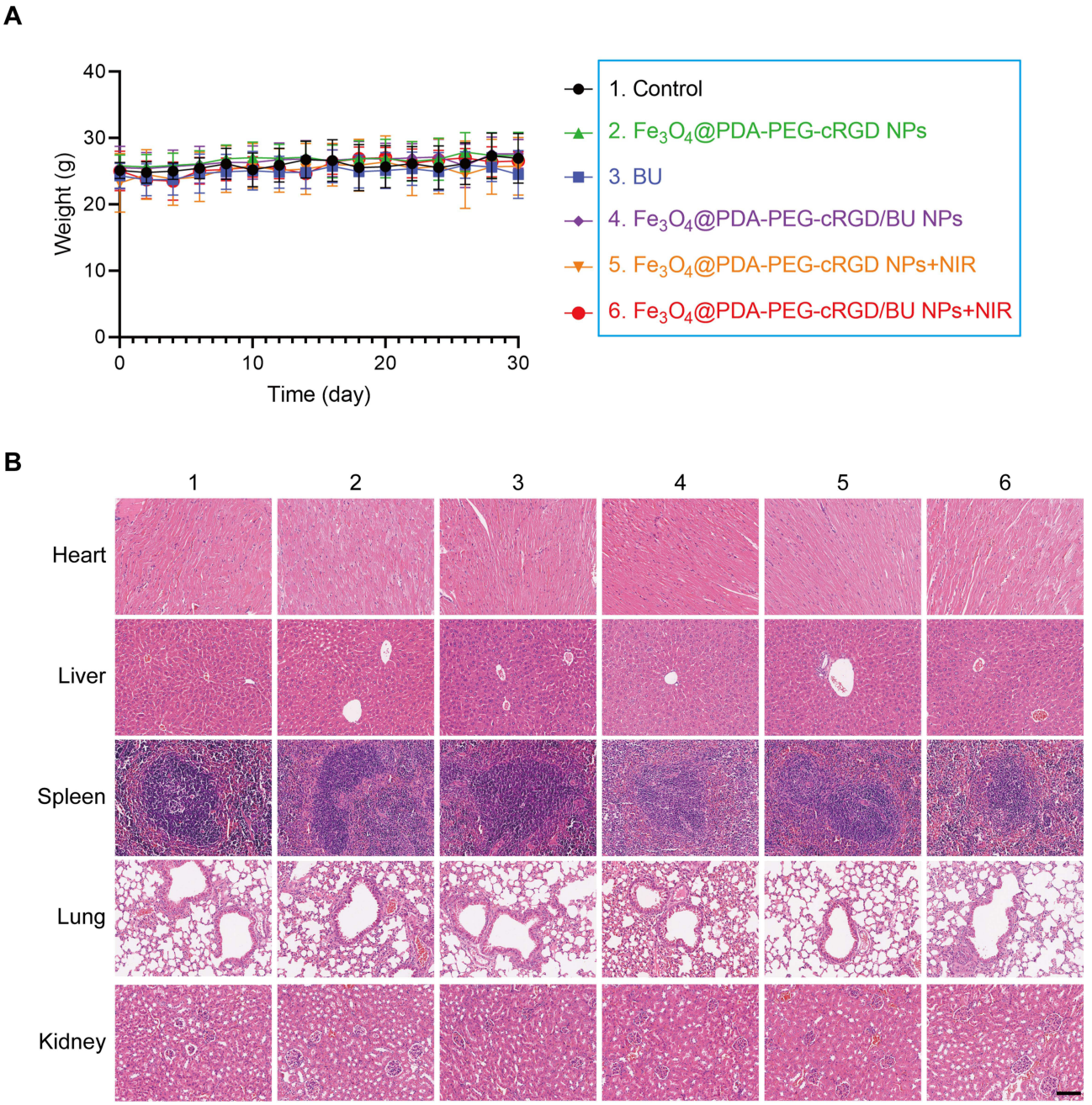

Figure 8 Biosafety assessment. (**A**) Body weight of HCT116 tumor-bearing mice after different treatments. (**B**) H&E staining results of main organs after treatments (scale bar=100 μm). (n=6).

Discussion

PTT has attracted widespread attention as a promising tumor treatment method, but its high temperature (>50°C) may cause adverse risks, including inflammatory disease and tumor metastasis. Therefore, mild PTT at a relatively low temperature (≤45°C) can avoid these drawbacks and provide a broader clinical application platform. However, HSPs (such as HSP70 and HSP90) are abnormally overexpressed and induce thermotolerance during mild PTT, which protects tumor cells from death, ultimately leading to the failure of mild PTT.[10,18–20] Consequently, researchers have aimed to overcome thermotolerance by inhibiting HSPs to improve the therapeutic efficiency of mild PTT.

Recently, thermotolerance has been overcome using various HSPs inhibition strategies based on the rapid development of nanomedicine, such as HSPs inhibitor-mediated HSPs inhibition,[49,50] gene editing-mediated HSPs

inhibition[35,51,52] and ATP-mediated HSPs inhibition.[17] For instance, Zhang et al synthesized a mitochondria-targeted photosensitizer consisting of IR780 iodide and BIIB021 (an HSP90 inhibitor). Under 808nm laser irradiation, BIIB021 was released from the prepared PEG-IR780-BIIB021 to inhibit HSP90 to increase tumor heat sensitivity, which achieved an excellent anti-tumor effect of mild PTT.[49] Ding et al designed a PEGylated PDA-coated siRNA-bearing nucleic acid nanogel (PEG-PDA-NG) with three shields (nucleic acid nanogel, PDA, and PEG) that protect siRNA from the degradation of lysosomes to silence HSP70, which achieve combinational effects of gene silencing and mild PTT.[35] Nevertheless, the use of HSP inhibitors is a hysteretic process, as they only act on existing HSPs, and the delivery and physiological stability of siRNA also impede its application. Therefore, research on alternative approaches to inhibit HSPs are necessary to potentiate the anti-tumor effect of mild PTT. Glycolysis is the main source of ATP in cancer cells and plays a pivotal role in the macromolecular biosynthesis of amino acids, fatty acids, and proteins.[53,54] Thus, inhibition of anaerobic glycolysis could decrease the production of ATP, which ultimately inhibits the synthesis of downstream metabolites such as HSPs.[23,24,55–57] Consequently, glycolysis suppression has been proposed to enhance the anti-tumor efficacy of mild PTT by inhibiting ATP-dependent HSPs generation.

BU is an active compound of the traditional Chinese medicine HuaChanSu[27] and exerts broad-spectrum anti-tumor effects, including inhibition of tumor cell proliferation, inhibition of angiogenesis, induction of apoptosis, and reversal of multidrug resistance.[29,41,58–62] In this study, we found that BU was significantly involved in the HIF-1 and glycolysis signaling pathways via transcriptomic analyses. In our previous study, we demonstrated that BU targeted the SRC-3/HIF-1α pathway to exert anti-tumor effect.[40] Therefore, we explored the relationship between the SRC-3/HIF-α pathway and glycolysis. Our results confirmed that BU reduced the expression of SRC-3, HIF-1α, and glycolytic proteins including GLUT1 and LDHA.[63] Thus, reducing GLUT1 and LDHA expression may effectively inhibit glycolysis. Glucose uptake, extracellular lactate, and intracellular ATP levels were also suppressed by BU, which confirmed that BU could inhibit glycolysis via the SRC-3/HIF-1α pathway.

Then, the effect of BU on HSPs was evaluated. HSP70 expression was inhibited in a concentration-dependent manner following BU treatment. The combination of BU and mild PTT was performed to demonstrate that blocking the expression of HSPs by inhibiting ATP generation via BU-mediated glycolysis suppression could effectively amplify the sensitivity of CRC toward mild PTT.

In addition, BU was specifically delivered to tumor cells using well-designed Fe_3O_4@PDA-PEG-cRGD/BU NPs. Under 808 nm NIR irradiation, Fe_3O_4@PDA-PEG-cRGD/BU NPs-mediated mild PTT triggered an effective anti-tumor effect both in vitro and in vivo, indicating that BU could overcome the thermal resistance and improve therapeutic efficacy. In details, Fe_3O_4@PDA-PEG-cRGD/BU NPs could target tumor cells, trigger the photothermal effect and release BU under NIR radiation. Subsequently, the released BU could directly target SRC-3 protein and regulate the expression of HIF-1α, which could downregulate GLUT1 and thereby inhibit the glucose metabolism and ATP-dependent HSP synthesis, and then sensitize tumors to mild PTT. Not only that, BU also exhibits the anti-tumor properties such as kill tumor cells directly, inhibit tumor angiogenesis, and reverse multidrug resistance.[29,41,58–62] Thus, Fe_3O_4@PDA-PEG-cRGD/BU NPs might display more advantages than other HSPs inhibition strategies.

Furthermore, as an excellent T_2-weighted MRI contrast agent, superparamagnetic Fe_3O_4 has been broadly applied in tumor diagnosis.[64–66] The superparamagnetic properties of the Fe_3O_4@PDA-PEG-cRGD/BU NPs were not affected by the PDA coating. The capability of the Fe_3O_4@PDA-PEG-cRGD/BU NPs for T_2-weighted MRI was verified both in vitro and in vivo. Therefore, Fe_3O_4@PDA-PEG-cRGD/BU NPs are ideal contrast agents for T_2-weighted MRI, which is conducive to accurate tumor diagnosis, and can guide the selection of time windows and real-time monitoring during cancer therapy.

Conclusion

In summary, BU inhibited anaerobic glycolysis by targeting the SRC-3/HIF-1α pathway, ultimately leading to a decrease in ATP-dependent HSPs synthesis, thus overcoming the main limitation of mild PTT in CRC. Furthermore, Fe_3O_4 @PDA-PEG-cRGD/BU NPs were designed to deliver BU to the tumor site and exhibited good tumor-targeting efficiency both in vitro and in vivo. Importantly, Fe_3O_4@PDA-PEG-cRGD/BU NPs reduced heat endurance by inhibiting over-expressed HSP70 and performed excellent anti-tumor efficacy of mild PTT. In addition, Fe_3O_4@PDA-PEG-cRGD/BU

NPs could be used for MRI. This study provides a highly effective strategy for enhancing the therapeutic effects of mild PTT and broadening the clinical applications of traditional Chinese medicine.

Acknowledgments

This work was supported by the National Nature Science Foundation of China (grant no. 81973700 and 81873137) and The Science and Technology Innovation Project of Shanghai Putuo District Health Commission (grant no. ptkwws202004), Clinical Specialized Discipline of Health System of Putuo District in Shanghai (grant no. 2021tszk01), and the Shanghai Key Medical Specialty Construction Project (grant no. ZK2019B18), Clinical Specialized Disease Construction Project of Shanghai Putuo District Municipal Health Commission (grant no. 2019tszb01), and National Key Research and Development Program of China (grant no. 2019YFC1316000). We also thank the funding support from the Fifth Batch of "Xinglin Scholar" of Shanghai University of Traditional Chinese Medicine and the Reserve Outstanding Chinese Medicine Talent of Shanghai University of Traditional Chinese Medicine.

Disclosure

The authors report no conflicts of interest in this work.

References

1. Sung H, Ferlay J, Siegel RL, et al. Global cancer statistics 2020: GLOBOCAN estimates of incidence and mortality worldwide for 36 cancers in 185 countries. *CA Cancer J Clin*. 2021;71(3):209–249. doi:10.3322/caac.21660
2. Arnold M, Sierra MS, Laversanne M, Soerjomataram I, Jemal A, Bray F. Global patterns and trends in colorectal cancer incidence and mortality. *Gut*. 2017;66(4):683–691. doi:10.1136/gutjnl-2015-310912
3. Ogura A, Konishi T, Cunningham C, et al. Neoadjuvant (Chemo)radiotherapy with total mesorectal excision only is not sufficient to prevent lateral local recurrence in enlarged nodes: results of the multicenter lateral node study of patients with low cT3/4 rectal cancer. *J Clin Oncol*. 2019;37(1):33–43. doi:10.1200/jco.18.00032
4. Picco G, Cattaneo CM, van Vliet EJ, et al. Werner helicase is a synthetic-lethal vulnerability in mismatch repair-deficient colorectal cancer refractory to targeted therapies, chemotherapy, and immunotherapy. *Cancer Discov*. 2021;11(8):1923–1937. doi:10.1158/2159-8290.Cd-20-1508
5. Johdi NA, Sukor NF. Colorectal Cancer Immunotherapy: options and Strategies. *Front Immunol*. 2020;11:1624. doi:10.3389/fimmu.2020.01624
6. Gao Q, Zhou G, Lin SJ, Paus R, Yue Z. How chemotherapy and radiotherapy damage the tissue: comparative biology lessons from feather and hair models. *Exp Dermatol*. 2019;28(4):413–418. doi:10.1111/exd.13846
7. Weng J, Li S, Zhu Z, et al. Exploring immunotherapy in colorectal cancer. *J Hematol Oncol*. 2022;15(1):95. doi:10.1186/s13045-022-01294-4
8. Xu C, Pu K. Second near-infrared photothermal materials for combinational nanotheranostics. *Chem Soc Rev*. 2021;50(2):1111–1137. doi:10.1039/d0cs00664e
9. Zhao L, Zhang X, Wang X, Guan X, Zhang W, Ma J. Recent advances in selective photothermal therapy of tumor. *J Nanobiotechnol*. 2021;19(1):335. doi:10.1186/s12951-021-01080-3
10. Gao G, Sun X, Liang G. Nanoagent-promoted mild-temperature photothermal therapy for cancer treatment. *Adv Funct Mater*. 2021;31(25):2100738. doi:10.1002/adfm.202100738
11. Jiang Z, Li T, Cheng H, et al. Nanomedicine potentiates mild photothermal therapy for tumor ablation. *Asian J Pharm Sci*. 2021;16(6):738–761. doi:10.1016/j.ajps.2021.10.001
12. Carmignani A, Battaglini M, Marino A, Pignatelli F, Ciofani G. Drug-loaded polydopamine nanoparticles for chemo/photothermal therapy against colorectal cancer cells. *ACS Appl Bio Mater*. 2024;7(4):2205–2217. doi:10.1021/acsabm.3c01203
13. Jiang Z, Wang Y, Sun L, et al. Dual ATP and pH responsive ZIF-90 nanosystem with favorable biocompatibility and facile post-modification improves therapeutic outcomes of triple negative breast cancer in vivo. *Biomaterials*. 2019;197:41–50. doi:10.1016/j.biomaterials.2019.01.001
14. Shao L, Li Y, Huang F, et al. Complementary autophagy inhibition and glucose metabolism with rattle-structured polydopamine@mesoporous silica nanoparticles for augmented low-temperature photothermal therapy and in vivo photoacoustic imaging. *Theranostics*. 2020;10(16):7273–7286. doi:10.7150/thno.44668
15. Zhang X, Du J, Guo Z, et al. Efficient near infrared light triggered nitric oxide release nanocomposites for sensitizing mild photothermal therapy. *Adv Sci*. 2019;6(3):1801122. doi:10.1002/advs.201801122
16. Yi X, Duan QY, Wu FG. Low-temperature photothermal therapy: strategies and applications. *Research*. 2021;2021:9816594. doi:10.34133/2021/9816594
17. He X, Zhang S, Tian Y, Cheng W, Jing H. Research progress of nanomedicine-based mild photothermal therapy in tumor. *Int J Nanomed*. 2023;18:1433–1468. doi:10.2147/ijn.S405020
18. Yang Y, Zhu W, Dong Z, et al. 1D coordination polymer nanofibers for low-temperature photothermal therapy. *Adv Mater*. 2017;29(40). doi:10.1002/adma.201703588
19. Horowitz M, Robinson SD. Heat shock proteins and the heat shock response during hyperthermia and its modulation by altered physiological conditions. *Prog Brain Res*. 2007;162:433–446. doi:10.1016/s0079-6123(06)62021-9
20. Shu X, Chen Y, Yan P, et al. Biomimetic nanoparticles for effective mild temperature photothermal therapy and multimodal imaging. *J Control Release*. 2022;347:270–281. doi:10.1016/j.jconrel.2022.05.010

21. Abi Zamer B, El-Huneidi W, Eladl MA, Muhammad JS. Ins and outs of heat shock proteins in colorectal carcinoma: its role in carcinogenesis and therapeutic perspectives. *Cells*. 2021;10(11). doi:10.3390/cells10112862
22. Cao Y, Ren Q, Hao R, Sun Z. Innovative strategies to boost photothermal therapy at mild temperature mediated by functional nanomaterials. *Mater Des*. 2022;214:110391.
23. Dai Y, Sun Z, Zhao H, et al. NIR-II fluorescence imaging guided tumor-specific NIR-II photothermal therapy enhanced by starvation mediated thermal sensitization strategy. *Biomaterials*. 2021;275:120935. doi:10.1016/j.biomaterials.2021.120935
24. Dang J, Ye H, Li Y, Liang Q, Li X, Yin L. Multivalency-assisted membrane-penetrating siRNA delivery sensitizes photothermal ablation via inhibition of tumor glycolysis metabolism. *Biomaterials*. 2019;223:119463. doi:10.1016/j.biomaterials.2019.119463
25. Warburg O. On respiratory impairment in cancer cells. *Science*. 1956;124(3215):269–270.
26. Luo Z, Xu J, Sun J, et al. Co-delivery of 2-Deoxyglucose and a glutamine metabolism inhibitor V9302 via a prodrug micellar formulation for synergistic targeting of metabolism in cancer. *Acta Biomater*. 2020;105:239–252. doi:10.1016/j.actbio.2020.01.019
27. Lee S, Lee Y, Choi YJ, Han KS, Chung HW. Cyto-/genotoxic effects of the ethanol extract of Chan Su, a traditional Chinese medicine, in human cancer cell lines. *J Ethnopharmacol*. 2014;152(2):372–376. doi:10.1016/j.jep.2014.01.023
28. Dou L, Zou D, Song F, Jin Y, Li Y, Zhang Y. Bufalin suppresses ovarian cancer cell proliferation via EGFR pathway. *Chin Med J*. 2021;135 (4):456–461. doi:10.1097/cm9.0000000000001879
29. Fang K, Zhan Y, Zhu R, et al. Bufalin suppresses tumour microenvironment-mediated angiogenesis by inhibiting the STAT3 signalling pathway. *J Transl Med*. 2021;19(1):383. doi:10.1186/s12967-021-03058-z
30. Yang L, Zhou F, Zhuang Y, et al. Acetyl-bufalin shows potent efficacy against non-small-cell lung cancer by targeting the CDK9/STAT3 signalling pathway. *Br J Cancer*. 2021;124(3):645–657. doi:10.1038/s41416-020-01135-6
31. Zou D, Song J, Deng M, et al. Bufalin inhibits peritoneal dissemination of gastric cancer through endothelial nitric oxide synthase-mitogen-activated protein kinases signaling pathway. *FASEB j*. 2021;35(5):e21601. doi:10.1096/fj.202002780R
32. Fu R, Yu F, Wu W, et al. Bufalin enhances the killing efficacy of NK cells against hepatocellular carcinoma by inhibiting MICA shedding. *Int Immunopharmacol*. 2021;101(Pt B):108195. doi:10.1016/j.intimp.2021.108195
33. Fan X, Yuan Z, Shou C, et al. cRGD-conjugated Fe(3)O(4)@PDA-DOX multifunctional nanocomposites for MRI and antitumor chemo-photothermal therapy. *Int J Nanomed*. 2019;14:9631–9645. doi:10.2147/ijn.S222797
34. Ni C, Lu J, Chen Z, et al. Preparation of polydopamine-based concave nanoparticles and mild photothermal-anti-inflammatory combination therapy for breast cancer guided by magnetic resonance imaging. *Mater Des*. 2023;229:111858. doi:10.1016/j.matdes.2023.111858
35. Ding F, Gao X, Huang X, et al. Polydopamine-coated nucleic acid nanogel for siRNA-mediated low-temperature photothermal therapy. *Biomaterials*. 2020;245:119976. doi:10.1016/j.biomaterials.2020.119976
36. Lu J, Cai L, Dai Y, et al. Polydopamine-based nanoparticles for photothermal therapy/chemotherapy and their synergistic therapy with autophagy inhibitor to promote antitumor treatment. *Chem Rec*. 2021;21(4):781–796. doi:10.1002/tcr.202000170
37. Carmignani A, Battaglini M, Bartolucci M, Petretto A, Prato M, Ciofani G. Polydopamine nanoparticles as a non-pharmaceutical tool in the treatment of fatty liver disease. *Mater Des*. 2024;239:112825. doi:10.1016/j.matdes.2024.112825
38. Carmignani A, Battaglini M, Sinibaldi E, et al. In vitro and ex vivo investigation of the effects of polydopamine nanoparticle size on their antioxidant and photothermal properties: implications for biomedical applications. *ACS Appl Nano Mater*. 2022;5(1):1702–1713. doi:10.1021/acsanm.1c04536
39. Bao X, Zhao J, Sun J, Hu M, Yang X. Polydopamine nanoparticles as efficient scavengers for reactive oxygen species in periodontal disease. *ACS Nano*. 2018;12(9):8882–8892. doi:10.1021/acsnano.8b04022
40. Yuan Z, Liu C, Sun Y, et al. Bufalin exacerbates Photodynamic therapy of colorectal cancer by targeting SRC-3/HIF-1α pathway. *Int J Pharm*. 2022;624:122018. doi:10.1016/j.ijpharm.2022.122018
41. Chen J, Wang H, Jia L, et al. Bufalin targets the SRC-3/MIF pathway in chemoresistant cells to regulate M2 macrophage polarization in colorectal cancer. *Cancer Lett*. 2021;513:63–74. doi:10.1016/j.canlet.2021.05.008
42. Wang Y, Lonard DM, Yu Y, et al. Bufalin is a potent small-molecule inhibitor of the steroid receptor coactivators SRC-3 and SRC-1. *Cancer Res*. 2014;74(5):1506–1517. doi:10.1158/0008-5472.CAN-13-2939
43. Zhao W, Chang C, Cui Y, et al. Steroid receptor coactivator-3 regulates glucose metabolism in bladder cancer cells through coactivation of hypoxia inducible factor 1alpha. *J Biol Chem*. 2014;289(16):11219–11229. doi:10.1074/jbc.M113.535989
44. Iyer NV, Kotch LE, Agani F, et al. Cellular and developmental control of O2 homeostasis by hypoxia-inducible factor 1 alpha. *Genes Dev*. 1998;12 (2):149–162. doi:10.1101/gad.12.2.149
45. Semenza GL. HIF-1: upstream and downstream of cancer metabolism. *Curr Opin Genet Dev*. 2010;20(1):51–56. doi:10.1016/j.gde.2009.10.009
46. Xu J, Sun Y, Yuan Z, et al. Bufalin-loaded CaP/DPPE-PEG-EGF nanospheres: preparation, cellular uptake, distribution, and anti-tumor effects. *J Biomed Nanotechnol*. 2019;15(2):329–339. doi:10.1166/jbn.2019.2681
47. Hu Q, Liang B, Sun Y, et al. Preparation of bufalin-loaded pluronic polyetherimide nanoparticles, cellular uptake, distribution, and effect on colorectal cancer. *Int J Nanomed*. 2014;9:4035–4041. doi:10.2147/IJN.S64708
48. Liu T, Yuan X, Jia T, et al. Polymeric prodrug of bufalin for increasing solubility and stability: synthesis and anticancer study in vitro and in vivo. *Int J Pharm*. 2016;506(1–2):382–393. doi:10.1016/j.ijpharm.2016.04.041
49. Zhang T, Wu B, Akakuru OU, et al. Hsp90 inhibitor-loaded IR780 micelles for mitochondria-targeted mild-temperature photothermal therapy in xenograft models of human breast cancer. *Cancer Lett*. 2021;500:41–50. doi:10.1016/j.canlet.2020.12.028
50. Sun Q, Tang K, Song L, et al. Covalent organic framework based nanoagent for enhanced mild-temperature photothermal therapy. *Biomater Sci*. 2021;9(23):7977–7983. doi:10.1039/d1bm01245b
51. Guo R, Tian Y, Yang Y, Jiang Q, Wang Y, Yang W. A Yolk–Shell nanoplatform for gene-silencing-enhanced photolytic ablation of cancer. *Adv Funct Mater*. 2018;28(14):1706398. doi:10.1002/adfm.201706398
52. Hu H, Yang N, Sun J, et al. Zn(ii)-Coordination-driven self-assembled nanoagents for multimodal imaging-guided photothermal/gene synergistic therapy. *Chem Sci*. 2022;13(24):7355–7364. doi:10.1039/d2sc01769e
53. Ganapathy-Kanniappan S, Geschwind JF. Tumor glycolysis as a target for cancer therapy: progress and prospects. *Mol Cancer*. 2013;12:152. doi:10.1186/1476-4598-12-152
54. Pavlova NN, Thompson CB. The emerging hallmarks of cancer metabolism. *Cell Metab*. 2016;23(1):27–47. doi:10.1016/j.cmet.2015.12.006

55. Gao G, Jiang Y-W, Guo Y, et al. Enzyme-mediated tumor starvation and phototherapy enhance mild-temperature photothermal therapy. *Adv Funct Mater*. 2020;30(16):1909391. doi:10.1002/adfm.201909391
56. Chen WH, Luo GF, Lei Q, et al. Overcoming the heat endurance of tumor cells by interfering with the anaerobic glycolysis metabolism for improved photothermal therapy. *ACS Nano*. 2017;11(2):1419–1431. doi:10.1021/acsnano.6b06658
57. Wu S, Zhang K, Liang Y, et al. Nano-enabled tumor systematic energy exhaustion via Zinc (II) interference mediated glycolysis inhibition and specific GLUT1 depletion. *Adv Sci*. 2022;9(7):e2103534. doi:10.1002/advs.202103534
58. Yu Z, Li Y, Li Y, et al. Bufalin stimulates antitumor immune response by driving tumor-infiltrating macrophage toward M1 phenotype in hepatocellular carcinoma. *J Immunother Cancer*. 2022;10(5). doi:10.1136/jitc-2021-004297
59. Zhan Y, Qiu Y, Wang H, et al. Bufalin reverses multidrug resistance by regulating stemness through the CD133/nuclear factor-kappaB/MDR1 pathway in colorectal cancer. *Cancer Sci*. 2020;111(5):1619–1630. doi:10.1111/cas.14345
60. Li H, Xie S, Liu X, et al. Matrine alters microRNA expression profiles in SGC-7901 human gastric cancer cells. *Oncol Rep*. 2014;32(5):2118–2126. doi:10.3892/or.2014.3447
61. Chen G, Zhang H, Sun H, et al. Bufalin targeting BFAR inhibits the occurrence and metastasis of gastric cancer through PI3K/AKT/mTOR signal pathway. *Apoptosis*. 2023;28(9–10):1390–1405. doi:10.1007/s10495-023-01855-z
62. Wang H, Chen J, Li S, et al. Bufalin reverses cancer-associated fibroblast-mediated colorectal cancer metastasis by inhibiting the STAT3 signaling pathway. *Apoptosis*. 2023;28(3–4):594–606. doi:10.1007/s10495-023-01819-3
63. Nagao A, Kobayashi M, Koyasu S, Chow CCT, Harada H. HIF-1-dependent reprogramming of glucose metabolic pathway of cancer cells and its therapeutic significance. *Int J Mol Sci*. 2019;20(2). doi:10.3390/ijms20020238
64. Jiang F, Wang L, Tang Y, et al. US/MR bimodal imaging-guided bio-targeting synergistic agent for tumor therapy. *Int J Nanomed*. 2022;17:2943–2960. doi:10.2147/ijn.S363645
65. Yao Y, Zhao D, Li N, et al. Multifunctional Fe(3)O(4)@Polydopamine@DNA-fueled molecular machine for magnetically targeted intracellular Zn (2+) imaging and fluorescence/MRI guided photodynamic-photothermal therapy. *Anal Chem*. 2019;91(12):7850–7857. doi:10.1021/acs.analchem.9b01591
66. Huang HC, Barua S, Sharma G, Dey SK, Rege K. Inorganic nanoparticles for cancer imaging and therapy. *J Control Release*. 2011;155(3):344–357. doi:10.1016/j.jconrel.2011.06.004